Robotics and Computer–Integrated Manufacturing 51 (2018) 37–52

Contents lists available at ScienceDirect

Robotics and Computer–Integrated Manufacturing

journal homepage: www.elsevier.com/locate/rcim

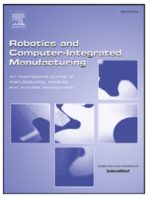

Full length Article

Modeling and experimental evaluation of an improved amphibious robot with compact structure

Shuxiang Guo [a,b,c], Yanlin He [a,b], Liwei Shi [a,b,*], Shaowu Pan [a,b], Rui Xiao [a,b], Kun Tang [a,b], Ping Guo [a,b]

[a] *The Institute of Advanced Biomedical Engineering System, School of Life Science, Beijing Institute of Technology, No.5, Zhongguancun South Street, Haidian District, Beijing 100081, China*

[b] *Key Laboratory of Convergence Medical Engineering System and Healthcare Technology, the Ministry of Industry and Information Technology, Beijing Institute of Technology, No.5, Zhongguancun South Street, Haidian District, Beijing 100081, China*

[c] *Faculty of Engineering, Kagawa University, 2217-20 Hayashi-cho, Takamatsu, Kagawa 760-8521, Japan*

ARTICLE INFO

Keywords:
Amphibious spherical robot
Hydrodynamic characteristics estimation
Kinematic analysis
Modified Denavit–Hartenberg method
ADAMS
ANSYS-FLUENT

ABSTRACT

This paper describes an improved three-dimensional (3D)-printed, low-cost, multi-functional, high-maneuverability, high-concealment, turtle-inspired mobile amphibious spherical robot for environmental monitoring and data collection. The major challenge in developing such a robot lies in its limited physical size and compact structure that allows for only one type of propulsion system to be used both on land and in water. This paper focuses on the optimization of the kinematic and hydrodynamic model of the amphibious spherical robot, so as to improve the control accuracy and stability of the robot. In order to optimize some kinematic and dynamic modeling parameters of the robot, such as the drag coefficient of robot, the angular velocity and swing angle of each joint, a solid model of the 3D-printed robot was built by SolidWorks. Our simulation results and theoretical calculations confirmed the validity of the virtual model and facilitated identification of key parameters in the design. The correctness of the modeling was demonstrated by the stability of consecutive crawling and underwater movements, providing a basis for driving and controlling methods for this amphibious robot, as well as guidance for the robot's gait trajectory. Combining the robot's crawling mechanism with related simulation results, an optimized prototype of the 3D-printed amphibious spherical robot was constructed. A series of crawling experiments on a common floor were performed with the improved robot prototype, which was also done using the previous robot. The results were evaluated by a novel optical positioning system, NDI Polaris. Moreover, several experiments were carried on land crawling and underwater swimming to verify the performance of the improved amphibious spherical robot. Comparison of experimental and simulation results demonstrated the improved robot had better amphibious motion performance, as well as more potentiality and applicability to the real structures.

1. Introduction

In an effort to build robots that can carry out sophisticated tasks or collect data from unstructured environments, researchers have continued to emulate living creatures and their materials, morphology, and movements. Over the last several years, mobile robots have provided more detailed and complex data, allowing scientists to develop new perceptions and deeper insights into the functioning of the numerous ecosystems on the planet. The use of mobile robots yields unprecedented precise measurements of environmental processes and pushes forward the frontiers of robotics and other sciences.

Amphibious robots have generated significant interest due to their wide range of potential applications; this is due to their ability to operate in various surroundings, with multiple functions and high maneuverability. As a typical example, high-durability, waterproof, snake-inspired robots propel themselves by undulation movements of their bodies on land and underwater [1]. Unlike snake robots, many amphibious robots use different propulsion methods to adapt to different environments. For example, the actuator of the "Whegs" amphibious robot is a combination of propellers and legs that allows the robot to move on rough terrain and in underwater environments [2]. AmphiRobot-II is an amphibious biomimetic fish-like robot with a wheel–propeller–fin mechanism and a specialized swivel mechanism [3]; specifically, the wheel–propeller–fin mechanism functions as a drive wheel for crawling on land and as a common screw propeller or pectoral fin in water. A salamander-like amphibious robot named Sala-mander Robot

---

[*] Corresponding author.
E-mail address: shiliwei@bit.edu.cn (L. Shi).

https://doi.org/10.1016/j.rcim.2017.11.009
Received 11 March 2016; Received in revised form 14 May 2017; Accepted 4 November 2017
0736-5845/© 2017 Elsevier Ltd. All rights reserved.

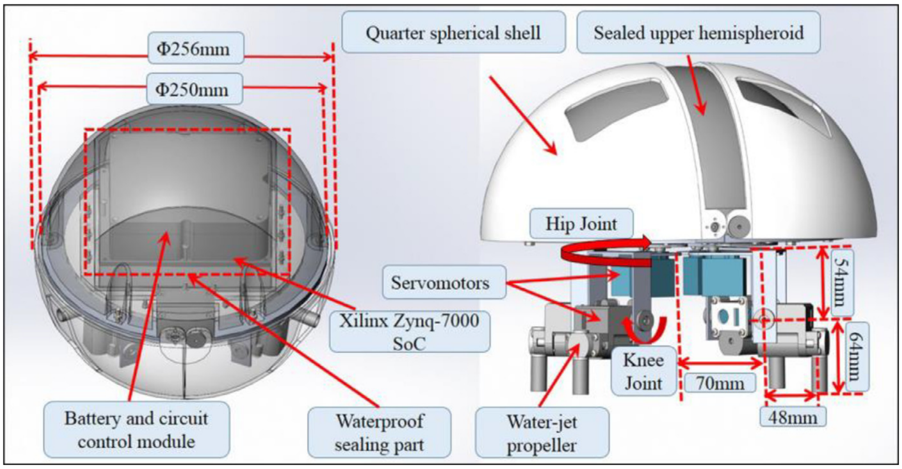

Fig. 1. Diagram of the improved three-dimensional (3D)-printed amphibious spherical robot.

mimics the terrestrial to aquatic locomotion transition via a combination of body undulation and limb crawling [4]. As mentioned above, there is also an amphibious mobile robot with a spherical rotary paddle mechanism, as shown in [5]. Each of these amphibious robots has its own characteristics and advantages. Wheeled robots have good performance on even ground, whereas tracked and legged robots have better mobility on rough terrain. Compared with screw propellers, undulatory and oscillatory propulsion with lower environmental disturbance can also achieve high efficiency and maneuverability. Some robots use two sets of propulsion mechanisms for terrestrial and aquatic motions, which lead to a heavier machine body. To simplify the structure, robots such as ACM-R5 and AQUA2 use composite propulsion mechanisms to move in amphibious environments.

However, it is still problematic for these amphibious robots to move in confined spaces. There are no manipulators on existing amphibious robots to improve mobility and flexibility for complex terrains on land or with underwater operations. Moreover, it is difficult for these amphibious robots to achieve accurate position control underwater via a swimming motion. For example, currents in the water prevent the amphibious robots without legs from retaining their position for precise manipulation. In our previous study, in an attempt to address some of the limitations of previous amphibious robot designs, we created a novel three-dimensional (3D) printing technology-based amphibious spherical robot with transformable composite propulsion mechanisms [6–8], to control and carry micro-robots. A spherical body provides maximum internal space and the advantages of flexibility, due to its symmetry both underwater and on land [9–15].

Traditional methods to design quadruped robots rely on mechanical prototype experimentation for design validation, which can be costly and time-consuming due to the numerous calculations involved and usually provides poor visualization outcomes. However, given the complex structure of the 3D-printed amphibious spherical robot, kinematic and hydrodynamic characterization is important for optimal performance. The kinematic model describes the relationship between the movement of each leg motion rod and the position and orientation of the end-actuator; a precise model is required for motion control and trajectory planning and is, thus, important basic work [16]. To date, numerous kinematic simulation studies have been performed [17–19]; some have focused on gait planning and control algorithms for an amphibious spherical robot [20]. For underwater robots, hydrodynamic characteristics are significant factors that directly affect the efficiency of the motion control algorithm; many researchers have studied the hydrodynamic characteristics of underwater robots and illustrated interaction effects [*e.g.*, 21–24]. These studies used many different methods for kinematic and hydrodynamic analyses to improve the robot's design efficiency and reliability.

In this paper, the kinematic and dynamic model of the amphibious spherical robot is optimized to provide some references for the controlling method and prototype production of the robot. Firstly, some on-land kinematic and dynamic modeling parameters are evaluated in ADAMS simulation. Then, in order to simplify the hydrodynamic model and improve the control accuracy and stability of the robot, some simulation analysis are carried out in ANSYS-FLUENT. Finally, several experiments are carried on land crawling and underwater swimming to verify the performance of the improved amphibious spherical robot. For the remaining sections of this paper in Section II the mechanical design and kinematic analysis of the improved 3D-printed amphibious spherical robot is described. Section III is dedicated to the kinematic simulation in ADAMS. Section IV discusses the hydrodynamic characteristics of the robot. The experimental validation is shown in Section V. Finally, Section VI presents the conclusions of this paper and future research directions.

2. Modeling and kinematic analysis of the robot

2.1. 3D-Printed amphibious spherical robot

As introduced in references [6,7], 3D printing technology was used to fabricate an amphibious spherical robot. We attempted to integrate the design and ensure seamless connections between every part to increase stability during the crawling process. To this end, and to avoid manual errors during fabrication, we sought to maximize the use of the upper hemispherical space and resources, to make the overall profile of the robot more compact and aesthetically pleasing. The diameter of the upper and lower hemisphere of this improved 3D-printed amphibious spherical robot is 250 mm and 256 mm respectively, the height of the actuating unit in standing state is 118 mm, the weight of the robot is approximately 2.26 kg, and the thickness of the spherical shell is 4 mm. Some more specifications of robot are shown in Fig. 1. The hip and knee joints of the robot have two active degrees of freedom (DOFs), referred to as the hip flexion and the knee flexion. The movement mechanisms of this improved 3D-printed amphibious spherical robot are the same as those presented in previous reports [10–12]. With adjustable complex actuation methods, the robot can change its movement mode between quadruped crawling and water-jet propulsion without manual manipulation. The robot walks on land by changing the gait of its four water-jet propellers as legs, with adjustment for the desired velocity. Simultaneously, by changing the directions and propulsive forces of its four water-jet propellers, the robot can not only move forward or backward but can also rotate clockwise or counterclockwise, with the ability to ascend, dive, or float in the underwater environment.

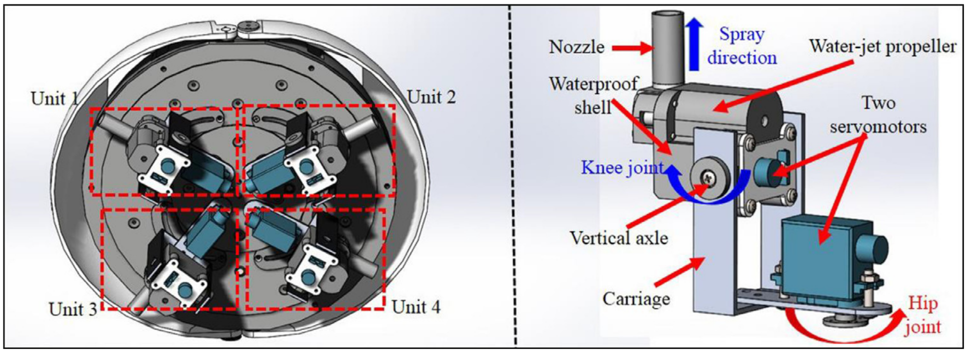

Fig. 2. Actuating system and a single actuating unit (leg).

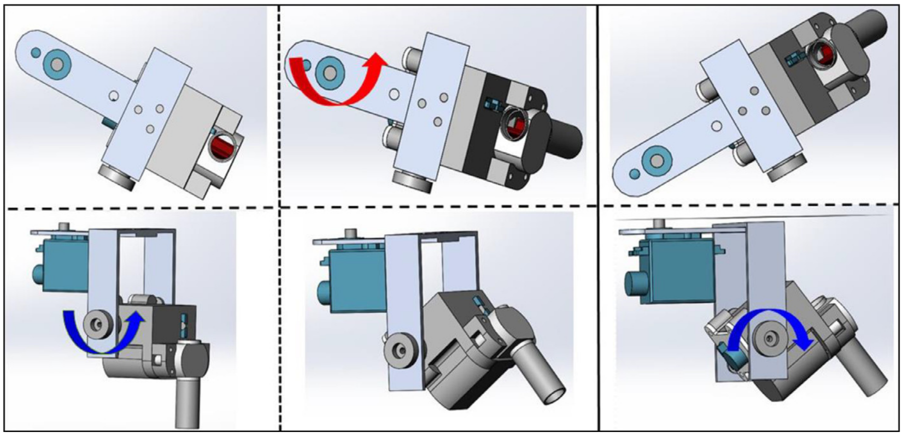

Fig. 3. The movement of a single leg.

Fig. 2 shows the whole structure of the four actuating system installed under the middle plate of the amphibious spherical robot and a single actuating unit. Actuating system is suspended under the middle plate by axles and controlled independently. Each unit (leg) is composed of one carriage, one water-jet propeller and two servo motors. As shown in Fig. 2, each unit (leg) has 2 degree of freedom, which can generate one more actuating force in water through water-jet mechanism. Here we use the HS-5086WP servo motors which have a compact size of $31^*15.2^*31$ mm. Each of them can rotate 120° in max and provide a maximum torch of $3.6\mathrm{kg}^*\mathrm{cm}$. The output of the eight PWM control signals is used to control eight servomotors of robot to implement the on-land crawling of the robot, where one cycle of the single unit is shown in Fig. 3. When the robot is in the underwater mode, the lower spherical shells will close. By changing the directions and propulsive forces of the robot's four water-jet propellers, the robot can motion underwater. The water-jet propeller is sized as 15^*21^*42 mm without nozzles, and a waterproof shell of servo motors and water-jet propellers are installed. With this structure, both vectored water-jet and quadruped crawling can be realized in one actuating system, this is why it is called a hybrid actuating system.

To decrease the power consumption of the integrated circuits (ICs) and promote modular design, an Avnet MicroZed core-board carrying a Xilinx all-programmable Zynq-7000 SoC (Z-7000) was adopted to prepare the electronic system of the improved version of this 3D-printed amphibious spherical robot. Zynq SoC provides an abundant set of power reduction mechanisms that cover various dynamical power management and dynamical voltage frequency scaling techniques. It is a hybrid processor combined with an advanced RISC machine (ARM) processor and field-programmable gate array (FPGA). The microcontroller provides eight pulse width modulation (PWM) signals to control the servo motors for crawling on land; four additional PWM signals are used to actuate the water-jet propellers by regulating the duty ratio of the PWM signal. Moreover, there are twelve general purpose input–output (GPIO) signals to control the optocoupler and relay, as shown in Fig. 4 [25].

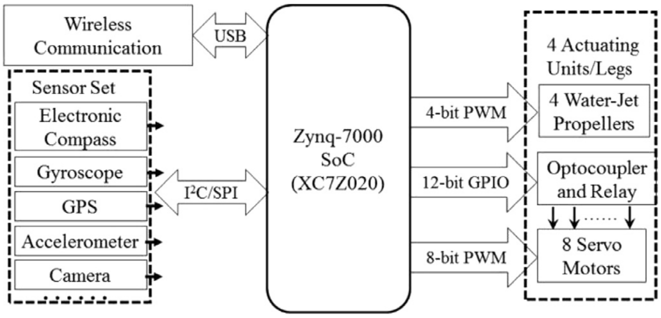

Fig. 4. Block diagram of the controller.

2.2. Relationship of kinematic parameters

To realize movement control and verify the kinematic characteristics of the robot, a Jacobian matrix based on the Denavit–Hartenberg parameters method was used to describe the relationship between velocity and angular velocity of the joint. The Jacobian matrix offers a theoretical foundation for subsequent simulation analysis based on a virtual prototype. Because the movement mechanism of the robot's four legs is basically the same, here, we present that for the right front leg as an example. In order to express the fixed coordinate system and kinematic parameters of the right front leg more clearly, we simplified the leg as two links (Link 2 and Link 3), as shown in Fig. 5. According to the rule of DH coordinates, the Link1 was assumed as a virtual link, and

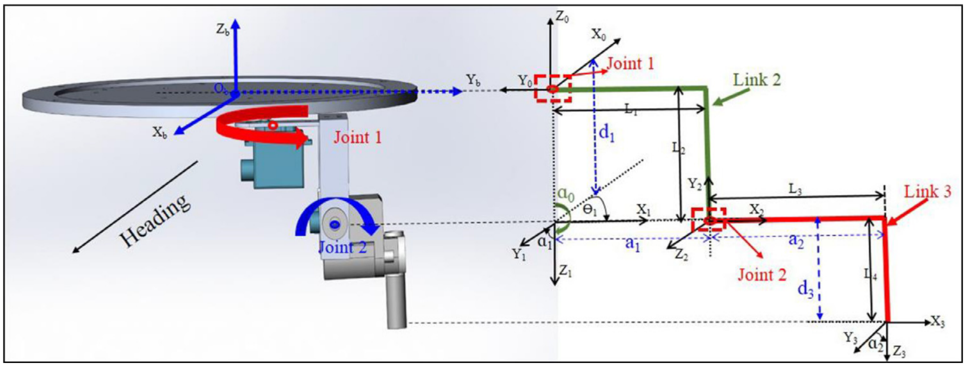

Fig. 5. Simplified Denavit–Hartenberg (DH) model of the right front leg.

Table 1
Denavit–Hartenberg (DH) parameters of the right front leg.

Link i	α_{i-1}	a_{i-1}	d_i	Θ_i
1	180^0	0	L_2	Θ_1
2	-90^0	L_1	0	Θ_2
3	90^0	L_3	L_4	0

it can be assumed as a point, the Link 2 consists of L_1 and L_2 and can be rotated in the $X_bO_bY_b$ plane, the Link 3 consists of L_3 and L_4, and can be rotated in the $Y_bO_bZ_b$ plane, L_i represents the length of the corresponding part, each leg is composed of a hip joint (joint1), a knee joint (joint2) and some connecting components.

Table 1 shows several related parameters of the right front leg, where a_{i-1} is the distance of the common normal from Z_{i-1} to Z_i, α_{i-1} is the angle about X_{i-1} from Z_{i-1} to Z_i, d_i is the distance of the common normal from X_{i-1} to X_i, Θ_i is the angle about Z_i from X_{i-1} to X_i [26,27].

In this paper, we consider a robot configuration in which the proper body fixed coordinate system (X_b, Y_b, Z_b) has its origin {O_b} located in the geometric center of the robot; the direction of X_b is the forward direction, and the negative direction of Z_b is in the direction of gravity. Thus, the positive direction of Y_b can be obtained by the right-hand rule. Assuming that the position vector of the hip joint for the right front leg in the coordinate system above is {x, y, z}, according to the homogeneous matrix transformation, the toe pose matrix of the amphibious spherical robot is given as follows:

$$\begin{aligned}
{}^b_3T &= {}^b_0T\,{}^0_3T = {}^b_0T\,{}^0_2T\,{}^2_3T = {}^b_0T\,{}^1_0T\,{}^1_2T\,{}^2_3T \\
&= \begin{bmatrix} 0 & -1 & 0 & x \\ -1 & 0 & 0 & y \\ 0 & 0 & 1 & z \\ 0 & 0 & 0 & 1 \end{bmatrix} * \begin{bmatrix} c_1c_2c_3 - s_1s_3 & -c_1c_2s_3 - s_1c_3 & c_1s_2 & c_1c_2l_3 + c_1s_2l_4 + c_1l_1 \\ -s_1c_2c_3 + c_1s_3 & s_1c_2s_3 + c_1c_2 & -s_1s_2 & -s_1c_2l_3 - s_1s_2l_4 - s_1l_1 \\ s_2c_3 & -s_2s_3 & -c_2 & s_2l_3 - c_2l_4 - l_2 \\ 0 & 0 & 0 & 1 \end{bmatrix} \\
&= \begin{bmatrix} s_1c_2c_3 - c_1s_3 & -s_1c_2s_3 - c_1c_2 & s_1s_2 & s_1c_2l_3 + s_1s_2l_4 + s_1l_1 + x \\ -c_1c_2c_3 + s_1s_3 & c_1c_2s_3 + s_1c_2 & -c_1s_2 & -c_1c_2l_3 - c_1s_2l_4 - c_1l_1 + y \\ s_2c_3 & -s_2s_3 & -c_2 & s_2l_3 - c_2l_4 - l_2 + z \\ 0 & 0 & 0 & 1 \end{bmatrix}
\end{aligned} \tag{1}$$

where c_i and s_i are defined as cos Θ_i and sin Θ_i, respectively. On the basis of the kinematic equations for the amphibious spherical robot, the position of the right toe in the body is given by

$${}^bp_{toe} = \begin{bmatrix} s_1c_2l_3 + s_1s_2l_4 + s_1l_1 + x \\ -c_1c_2l_3 - c_1s_2l_4 - c_1l_1 + y \\ s_2l_3 - c_2l_4 - l_2 + z \end{bmatrix} \tag{2}$$

The Jacobian matrix reveals the mapping relationship between the velocity of the end-effector and the angular velocity of each joint. If we determine the angular velocity of each joint, we could calculate the velocity of the end-effector. Thus, this approach offers a theoretical foundation for the simulation analysis based on the virtual prototype in ADAMS. The Jacobian matrix of the amphibious spherical robot can be formulated as

$$J = \begin{bmatrix} c_1c_2l_3 + c_1s_2l_4 + c_1l_1 & -s_1s_2l_3 + s_1c_2l_4 \\ s_1c_2l_3 + s_1s_2l_4 + s_1l_1 & c_1s_2l_3 - c_1c_2l_{41} \\ 0 & c_2l_3 + s_2l_4 \end{bmatrix} \tag{3}$$

According to the positive kinematics of a quadruped robot, assuming that the position of a servo-actuator can be described by the relative coordinates location vector $\mathrm{p} = \{\mathrm{p_x}, \mathrm{p_y}, \mathrm{p_z}\}^{\mathrm{T}}$, then the joint angles of the amphibious spherical robot are as given as follows:

$$\theta_1 = \arctan(-p_y/p_x) \tag{4}$$

$$\theta_2 = \arctan 2(\pm\sqrt{1 - t^2}, t) - \arctan 2\left(p_z, k\right) \tag{5}$$

$$t = \left(r - l_1\right)^2 + p_z^2 + l_4^2 - l_3^2/2l_4, \quad k = \sqrt{p_x^2 + p_y^2} - l_1,$$

$$r = \sqrt{p_x^2 + p_y^2}$$

Similarly, the kinematics of the three other legs can be obtained by the same method. For the sake of expressing the kinematics of the amphibious spherical robot more intuitively and concisely, here we set $\mathrm{q} = [\Theta_1, \Theta_2, \Theta_3]^{\mathrm{T}}$. The positive kinematics can then be expressed as

$${}^bp_{toe} = K^F(q) \tag{6}$$

Correspondingly, the inverse kinematics equations of the amphibious spherical robot are given by the following:

$$q = K_1\left({}^bp_{toe}\right) \tag{7}$$

3. Kinematic simulation in the ADAMS environment

To verify the stability of the robot's movement and the rationality of its structural design, as well as setting up the right rotation angle of the knee joint and hip joint, in this section, we modeled a virtual

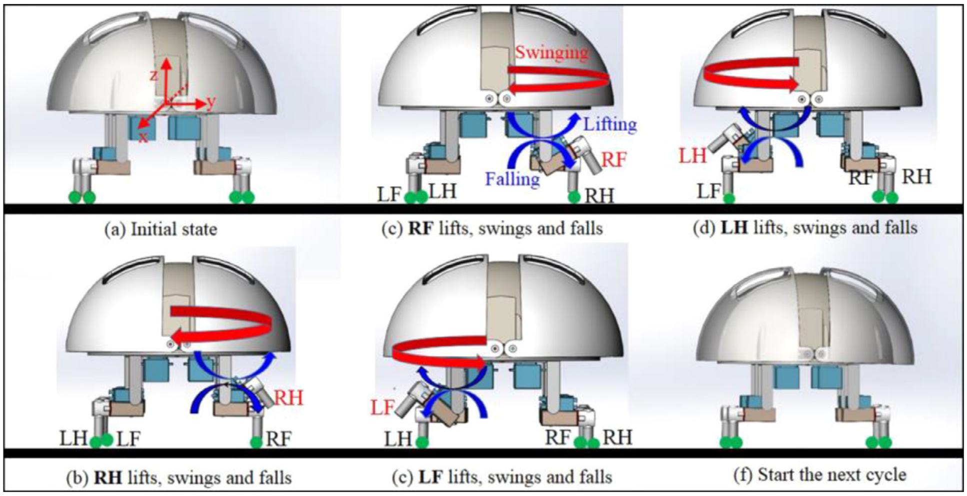

Fig. 6. Crawling gait of amphibious spherical robot within one cycle. (For interpretation of the references to colour in this figure legend, the reader is referred to the web version of this article.)

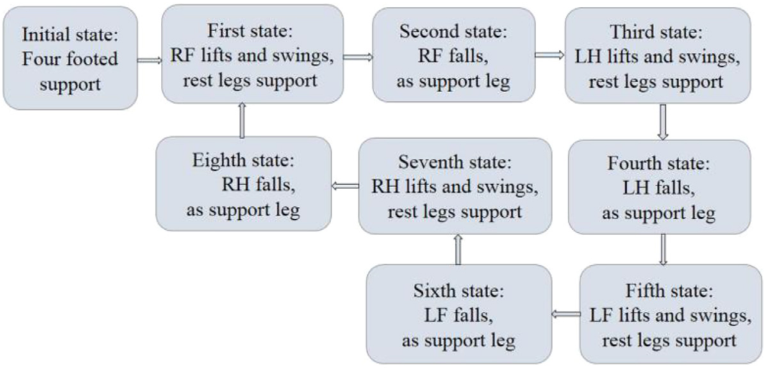

Fig. 7. Flow chart of crawling gait.

prototype of the amphibious spherical robot under the ADAMS environment. There are two methods for the establishment of a virtual prototype model in ADAMS: one is to build the 3D model in ADAMS directly and the other is to build the model using different 3D modeling software (*e.g.*, SolidWorks, Pro/E, and UG) and then import it into ADAMS. Although ADAMS has a powerful simulation analysis function, it has weaker entity modeling functions [28]. Taking into account precise simulation results in the presence of material non-linearities and distributed loads, we used the second method to build our robot model. First, a 3D model of the robot was established and simplified in SolidWorks; the format of the model was saved as a parasolid (*.xt). Second, the simplified 3D model of the robot was imported into ADAMS. Given that the simplified 3D model of the robot will lose some parameters, such as weight and the center of gravity, it was necessary to redefine these parameters. Moreover, some related constraints, motion function, and forces must be applied to the virtual prototype model.

The gait of a quadruped robot can be divided into four kinds: crawling, pacing, trotting, and gallop [27–30]. If the robot adopts a pacing gait or a gallop gait to walk, it will produce serious tilt against the robotic control. Moreover, with pacing and gallop gaits, it is easier to cause wear and tear to the spray pipe. Thus, a stable crawling gait was selected in this study. Fig. 6 shows that as the amphibious spherical robot completes a cycle of crawling, one of the legs is in a lifting and swinging state, and the other three legs are in a supporting state to provide balance and stability to the robot. In Fig. 6, LF is the left front leg, LH is the left hind leg, RF is the right front leg and LH is the right hind leg, the upper arrows indicate that the swing direction of joint, and the dots represent that the leg contact with ground, and the black stripes represents the ground. Details of the crawling motion are shown in Fig. 7, from the initial state (a four-footed support state) to the final state (eighth state-motion leg lift and swing while the other legs are in a support state).

By applying several related constraints and driving force to the virtual prototype model, its actual crawling gait was simulated in ADAMS, as shown in Fig. 8(a). From this figure, each leg has two DOFs: outward swaying freedom for the hip joint and rolling freedom of the knee joint. Consequently, each hip joint adds one revolving (horizontal rotation) DOF, and each knee joint adds one revolving (longitudinal rotation) DOF [30]. As mentioned above, the movement of the robot is driven by servo motors; thus, the drive function to each of the eight servo motors must be appended. The initial state of the robot was set as four-footed support state, the robot was assumed to be crawling on a broad ground, and the contact force between the foot end and the ground was set as the friction force. Considering the environment of the final experiment and the material of the foot end, the dynamic and static coefficient of friction forces were set as 0.1 and 0.15 respectively, as shown in Fig. 8(b). In the process of the robot crawling, each leg performs a series of cycles–“lift–swing–fall–support.”

After the robot completed a movement cycle in the crawling gait, the simulation animation results could be viewed in the post-processing module of ADAMS. Simultaneously, the displacement curves of the centroid, the driving torque of each joint, and the angular velocity and angular acceleration of each joint could be obtained during the simulation process [31–33].

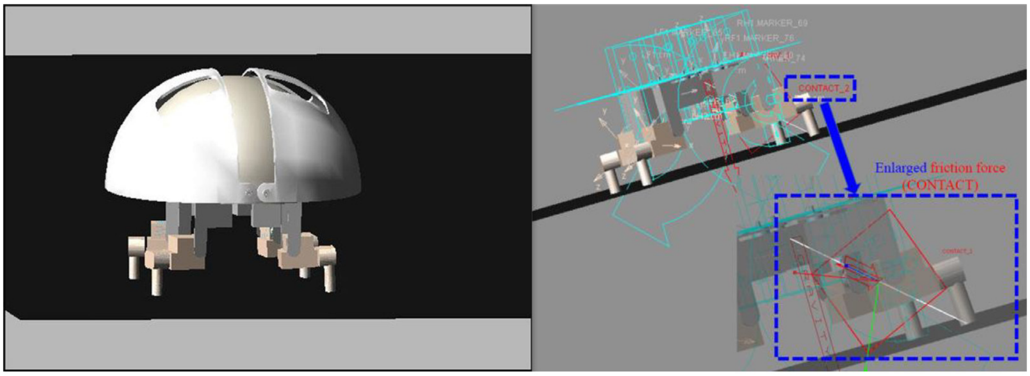

(a) Virtual environment of crawling

(b) Details of constraints

Fig. 8. Virtual prototype model of robot based on ADAMS platform.

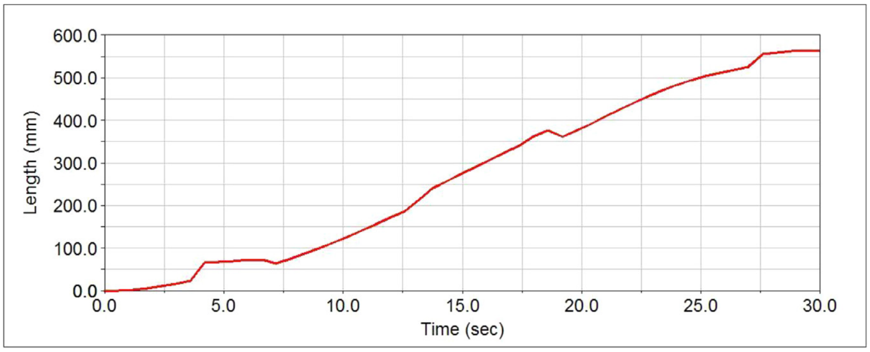

Fig. 9. Displacement curve of the centroid in the X direction.

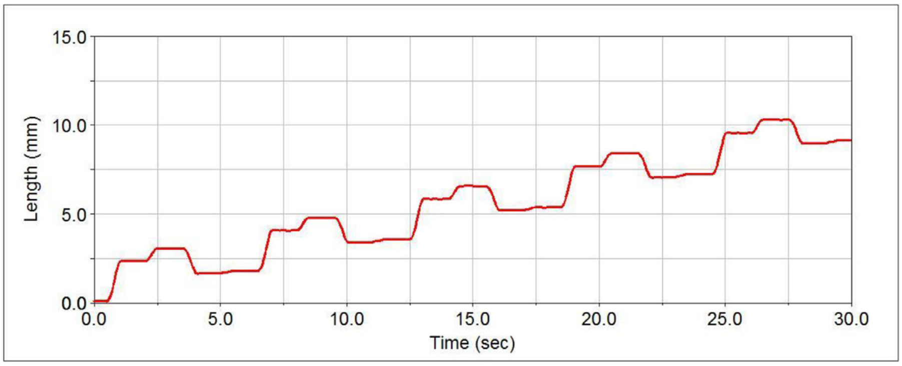

Fig. 10. Displacement curve of the centroid in the Y direction.

3.1. Simulation results of the displacement of the centroid

Through the post-processing function of ADAMS/View, and after determining the angle of the hip joint and knee joint, the moving trajectory of the centroid of the robot was obtained. These movement trajectories also demonstrate the velocity and stability of the robot (Figs. 9–11).

In Fig. 9, we see that the change in the centroid displacement in the X direction is stable, and the gradient remained close to 0.025. This curve shows the displacement in the heading direction of robot, the gradient represents the velocity of the robot; thus, this result showed that the velocity of the robot remained stable in the process of crawling and was basically maintained at around 0.025 m/s. Fig. 10 shows the centroid displacement curve in the Y direction and this displacement curve indicates the deviation of the robot in its horizontal direction. Left and right deviation can occur with robot crawling (Fig. 10) and the maximum deviation of the robot was approximately 0.011 m. Consequently, the final trajectory still follows the initial setting basically despite some deviations during crawling. The displacement curve of the centroid in the Z direction represents the phenomenon of the bumping up and down of the robot; the results showed that the translocation basically remain at 0.007 m which is about 2.5% of the height of the amphibious spherical robot (approximately 0.27 m, Fig. 11). Consequently, jumping and sudden changes should not appear, and the robot can implement stable crawling.

3.2. Simulation results of driving torque

Given that the joint motion of the robot depends on its driving force and torque, and the selection of the servo motor has a strong relationship with the driving torque, the size of the driving torque should be sufficient and reliable. Here, we only show the right front leg and left hind leg of the amphibious spherical robot as examples. Through the post-processing function of ADAMS, simulation results of driving torque of the joints are shown in Figs. 12 and 13 with respect to the hip joints and

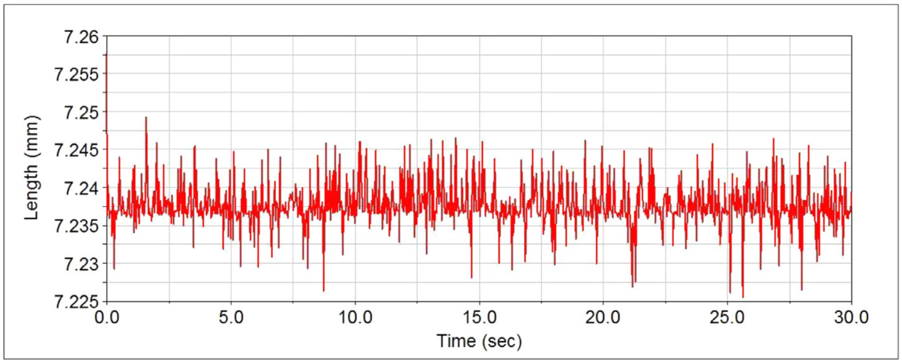

Fig. 11. Displacement curve of the centroid in the *Z* direction.

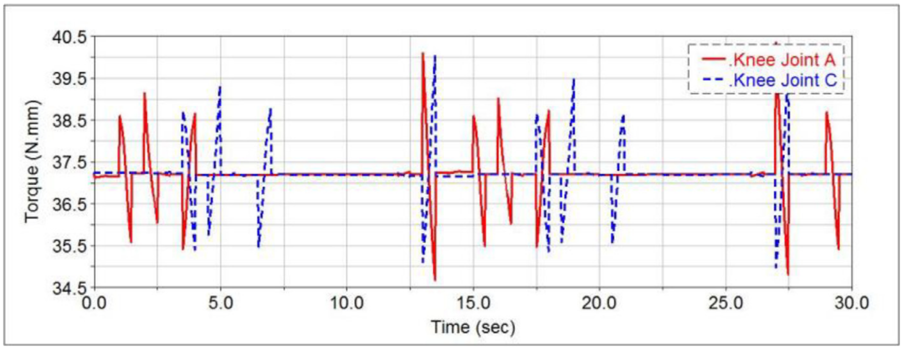

Fig. 12. Driving torque of the knee joint. (For interpretation of the references to colour in this figure legend, the reader is referred to the web version of this article.)

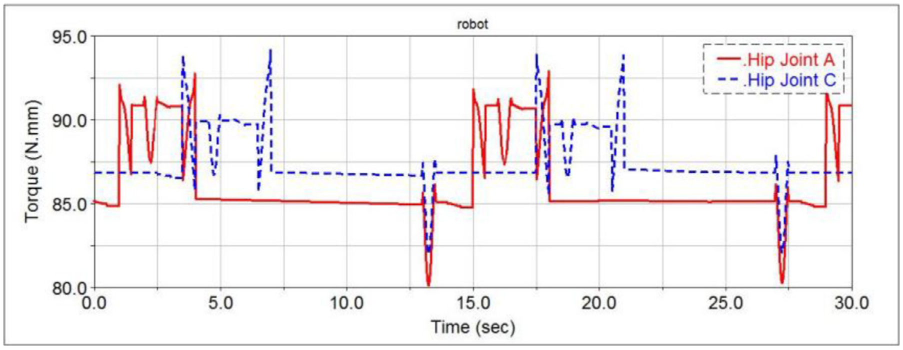

Fig. 13. Driving torque of the hip joint. (For interpretation of the references to colour in this figure legend, the reader is referred to the web version of this article.)

knee joints, respectively. The solid line indicates the driving torque of the knee joint A, and the dashed line indicates the driving torque of the knee joint C, as shown in Fig. 12. Similarly, the solid line in Fig. 13 indicates the driving torque of hip joint A, and the dashed line in Fig. 13 indicates the driving torque of hip joint C.

From these two figures we can draw the following conclusions. First, the driving torque of the hip joint is greater than that of the knee joint; this is due to the movement of the hip joint bringing about movement of the knee joint. The curves of driving torque appear abrupt and form spikes, which will induce unbalanced moment, impacting the stability of the amphibious spherical robot. Second, the driving torque of the supporting phase is much greater than in the swing phase; this is because the joint needs to bear part of the body load when the leg is in the support phase. Third, the maximum driving torque of the hip joint basically remained steady, below 94 N mm, when the hip joint was in the supporting phase, and the maximum driving torque of the knee joint remained steady, below 40 N mm. More importantly, little variation in the amplitude of each joint's driving torque was observed (*i.e.*, it did not generate excessive or too little torque).

3.3. Simulation results of angular velocity and angular acceleration

In the crawling process of the robot, the requirements for its movement are smooth, continuous, and without severe disruptions. The displacement trajectory of the centroid and toe of the robot were measured above. In addition to the requirements for displacement, the angular velocity and angular acceleration of each joint also have certain requirements: slow changes, smooth transitions, and the absence of severe disruptions. We assessed the angular velocity and angular acceleration of each joint.

Figs. 14 and 15 show the angular velocities of the knee joint and hip joint respectively. Figs. 16 and 17 show the angular acceleration of the knee joint and hip joint respectively. In these figures, different colors correspond to different joints. As shown in Figs. 14 and 15, the angular velocity and acceleration showed periodic changes to the knee joint. Over a period of time, the angular velocity show two major changes as the robot leg is lifted up and down. Here we select leg B as an example without loss of generality, the time periods of these two major changes occurred over the 3.5–4.0 s and 6.5–7.0 s periods respectively. In the

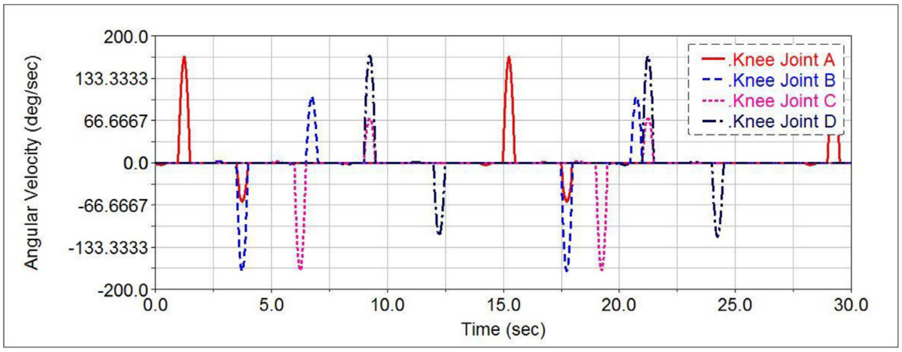

Fig. 14. Angular velocity of the knee joint.

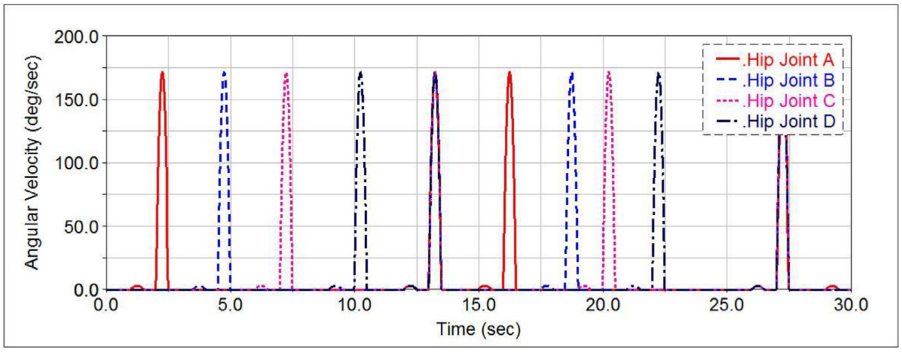

Fig. 15. Angular velocity of the hip joint.

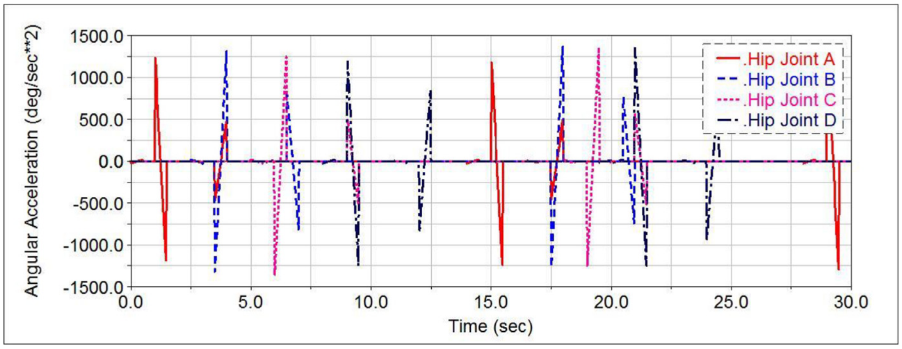

Fig. 16. Angular acceleration of the knee joint.

time period from 3.5–4.0 s, the leg B lifts its knee joint, as then the angular velocity of the knee joint increases first and decreases later. In the time period from 6.5–7.0 s, the leg B falls its knee joint; the angular velocity of knee joint reversely increases first and then decreases. For the hip joint, the angular velocity also shows the changes as the robot leg is swing forward. Besides, the angular acceleration is the rate of change of angular velocity. Due to the impact of contacting the ground by the supporting legs, there also exists some small changes of the angular velocity, and the impact problem must be considered in the actual selection of a drive servo motor. Moreover, through the angular velocity of each joint during simulation as shown in Figs. 14 and 15, we can calculate the velocity of robot at any time according to the Jacobian matrix.

4. Hydrodynamic analysis using ANSYS-FLUENT software

Hydrodynamic characteristics are a key parameter that determines the efficiency and accuracy of the control algorithms for a vehicle operating in an underwater environment. Moreover, to optimize the structure of the underwater robot, taking into consideration that the hydrodynamic characteristics of an underwater robot are different for each motion, a unique propulsion system is required for the 3D-printed amphibious spherical robot. Accordingly, hydrodynamic analysis is an important requirement for the motion control system of this robot, because water flows through four holes in the robot's hull during horizontal motion, and the streaming fluid is affected by the fin around the robot's equator. Also, the propulsive force influences the flexibility of the robot. Consequently, several vital hydrodynamic parameters of the robot were obtained from the analysis that have direct effects on the efficiency and performance of the robot. To estimate the parameters of dynamic model of robot, we assumed that the robot was a static sphere and the environment of flow field was 20°C without external disturbances.

4.1. Mechanism of underwater movement

It is a complex matter to design, analyze, and control soft robotic manipulators, due to the lack of an accurate dynamic model. Previous researchers have often used finite element and static structures. However, the description with such models is inaccurate for some of the features of the non-linear, transformable composite propulsion mechanism; also, complex water resistance effects are an important consid-

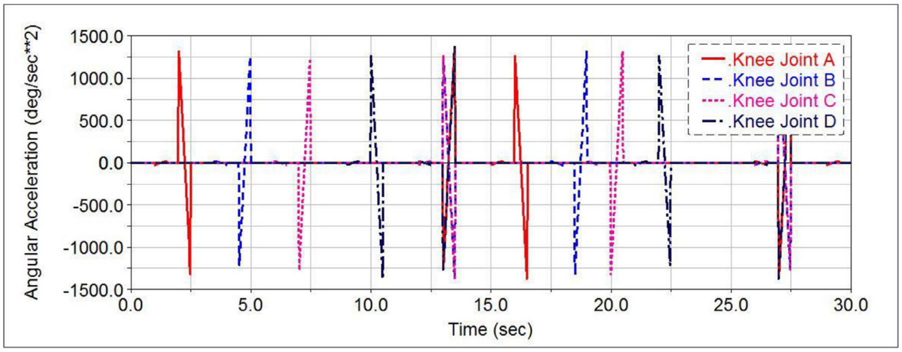

Fig. 17. Angular acceleration of the hip joint.

eration in these systems. In this paper, a hydrodynamic approach was used to model four kinds of motion, considering the propulsive forces and water resistance. By changing the directions and propulsive forces of the robot's four water-jet propellers, the robot can move not only forward or backward but can also rotate clockwise or counterclockwise, with the ability to ascend or dive underwater. In the horizontal plane, the robot adjusts a pair of water-jet propellers to implement forward and rotational motion. In the vertical plane, adjustment of the four water-jet propellers allows ascending or sinking motion. Fig. 18(a)–(d) shows a bottom view of the robot and the movement mechanism of one leg while implementing different movements. In these figures, F1, F2, and F3 are the thrusts generated by the water-jet propeller; T1, T2, and T3 are the corresponding torques of the motor, respectively; the linear arrows indicate the water-jet direction [34].

It has been suggested from studies of received biases that the robot is actuated by water-jet propellers when underwater [35]. Generally, the movement of the robot is subject to the different spray angles of the water-jet propellers. The force analysis provides an estimate for the requirements of the servo motors on the actuator units. Fig. 19 shows the force analysis for one actuator unit during different motions, such as horizontal forward motion, rotating motion, vertical ascending motion, and vertical sinking motion. By changing the angle of the vertical servo motor, thrust can be realized in any direction. The torque of the motor can be calculated as follows:

$$\begin{aligned} T_1 &= T_2 = F_1 L = F_2 L = L\rho A V_a^2 = L\left(k_1 V_i + k_2 V_c\right) \\ &= L\left(k_1 V_f \cos\theta + k_2 \frac{1}{2} D\Omega\right) \\ &= \frac{1}{4} L\rho\pi D^2\left(k_1^2 V_i^2 + k_1 k_2 \pi D^2 V_i + \frac{1}{4} k_2^2 D^2 \Omega^2\right) \end{aligned} \tag{8}$$

$$T_3 = F_3 L = L\rho A V_c^2 = \frac{1}{4} L\rho A D^2 \Omega^2 = \frac{1}{16} L\rho\pi D^4 \Omega^2 \tag{9}$$

The thrusts generated by the water-jet propellers are F1, F2 and F3; T1, T2, and T3 are the corresponding torques on the servo motor, respectively. L is the moment arm of the vertical motor, and ρ is the density of the fluid. According to previous studies [35], in the nozzle view of the small diameter, the velocity difference across the nozzle can be ignored. Thus, the axis flow velocity *Va* is a linear combination of the incoming flow velocity *Vi* and the central flow velocity *Vc*. Ω is the rotational velocity of the motor shaft, *Vf* is the velocity of the ambient flow, *Vi* is the velocity of the incoming flow, *Vo* is the velocity of the outlet flow, *Θ* is the incoming angle of the ambient flow, and *D* is the diameter of the nozzle.

Previous studies on amphibious spherical robots underwater emphasized a low speed state; thus, the 3D-printed amphibious spherical robot in this research was assumed to operate with low-speed motion. Accordingly, while the robot is in the process of underwater movement, the secondary drag force and linear damping force are two fundamental forces that must be taken into consideration. Thus, it is assumed that

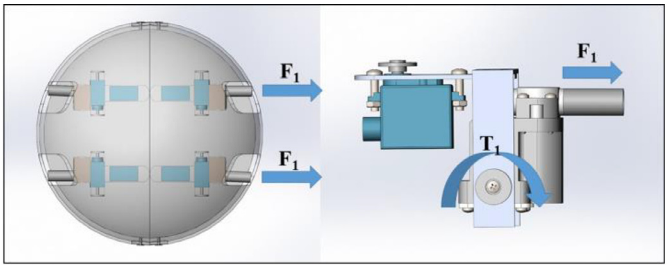

(a) Forward motion

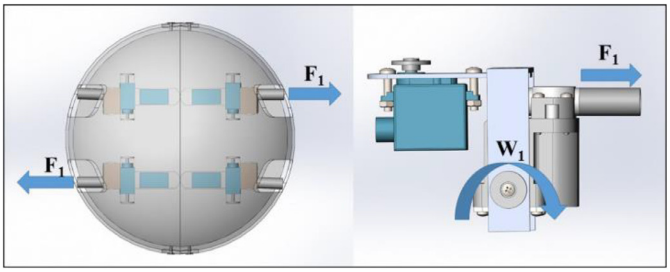

(b) Counter-clockwise rotation

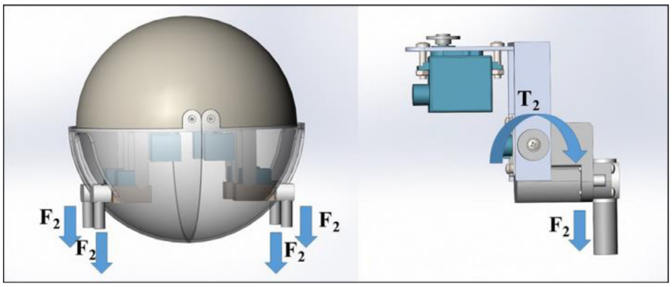

(c) Ascending motion

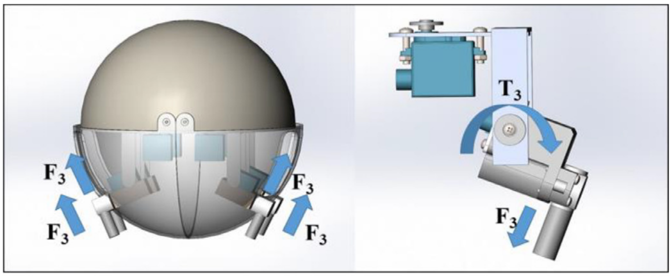

(d) Sinking motion

Fig. 18. Mechanisms of different underwater motions. (For interpretation of the references to colour in this figure legend, the reader is referred to the web version of this article.)

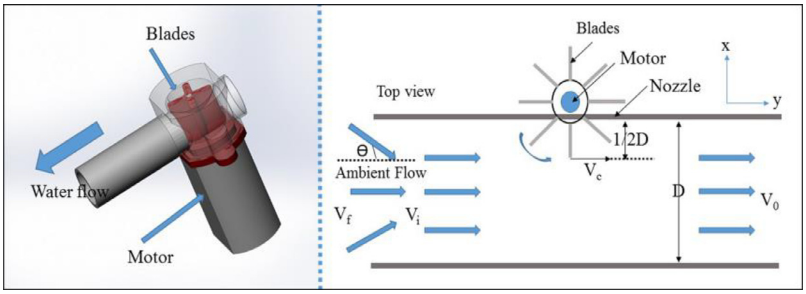

Fig. 19. Fluid model of a water-jet propeller [35].

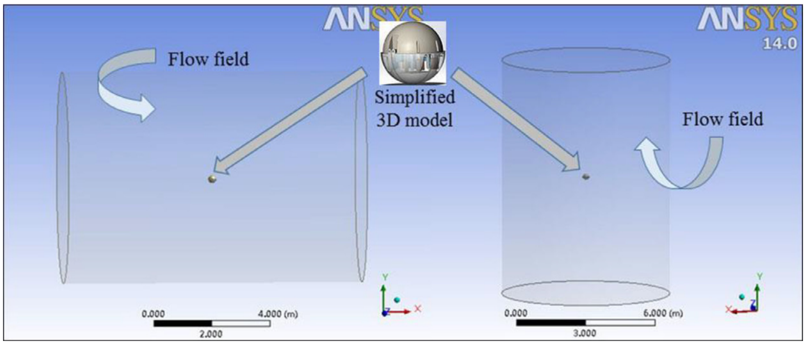

Fig. 20. Simplified 3D model in different flow field.

Table 2

Variation in drag coefficient with Reynolds numbers for a spherical particle.

Reynolds number R_e	R_e <10	10^3<R_e <3*10^5	R_e >3*10^5
Drag coefficient C_d	$20.4/R_e$	0.4	0.1

the velocity of fluid area is low; thus, the secondary drag force of the amphibious spherical underwater robot is given by

$$D_q(v)v = F_d = \frac{1}{2}C_d\left(R_e\right)\rho V^2 S \tag{10}$$

where R_e is the Reynolds number, ρ is the density of the fluid, V is the relative velocity of the robot to the fluid, S is the cross-sectional area, and F_d is the thrust force, also equivalent to the water resistance. C_d is the drag coefficient, which is different in the vertical and horizontal directions. As a spherical object in the vertical direction, C_d is equal to 0.4. In the horizontal direction, we can calculate the drag coefficient C_d according to (3). Moreover, the drag coefficient of the spherical particle is determined by the Reynolds number R_e, given by Eq. (10):

$$C_d = \frac{2T}{\rho V^2 S} \tag{11}$$

$$R_e = \frac{VD}{\mu} \tag{12}$$

where μ is the viscosity coefficient, which is 1×10^{-6} at 200 °C. In this study, the maximum simulation velocity of the amphibious spherical robot is 0.3 m/s; thus, the Reynolds number is $R_e = 1.2\times10^5$, which indicates that the flow is turbulent when the robot moves through the water. According to Table 2, C_d=0.4 when the Reynolds number is $R_e = 1.2\times10^5$. For vertical ascending and sinking motions, the propulsive forces are approximately 6.93 N and 1.061 N, respectively. For horizontal forward motion and counterclockwise rotation, fluid flows through the holes, such that the robot cannot be classified as closed. After comparing the two values of the drag coefficient, it is clear that the holes in the spherical hull increase the water resistance. Accordingly, by applying Eq. (10), D_q is 33.24 while the robot implements vertical ascending and sinking motions. Moreover, for horizontal forward motion and counterclockwise motion, D_q is 25.13, resulting in the following [36]:

$$D_q(v) = \begin{bmatrix} 25.13 & 0 & 0 & 0 & 0 & 0 \\ 0 & 25.13 & 0 & 0 & 0 & 0 \\ 0 & 0 & 33.24 & 0 & 0 & 0 \\ 0 & 0 & 0 & 0 & 0 & 0 \\ 0 & 0 & 0 & 0 & 0 & 0 \\ 0 & 0 & 0 & 0 & 0 & 0 \end{bmatrix} \begin{bmatrix} \mu \\ v \\ w \\ p \\ q \\ r \end{bmatrix}$$

4.2. Hydrodynamic simulation results

In this section, the influence of the flow field from the amphibious spherical robot is considered in the hydrodynamic analysis. The flow field used in this simulation must be built, based on the 3D model of the robot. The size of the flow field should be sufficiently large to ensure that the wall of the flow field cannot affect the hydrodynamic analysis results. Generally, the size and the shape of the flow field are determined by the robot. If the speed of the robot is relatively high and has a significant effect on the flow field, then we should choose a large flow field. A Boolean operation was then carried out between the 3D model and the flow field. The 3D model of the robot was subtracted from the flow field [36] to obtain the hydrodynamic analysis object, as shown in Fig. 20; an additional four 3D models were obtained applying the same method. In total, there were four objects to represent the four basic motions in the analysis.

In much of the previous work on hydrodynamic analyses, the mesh of the amphibious spherical robot and the flow field were determined to be key factors. Moreover, the overall amount of the mesh determines the effectiveness of the hydrodynamic analysis and the computational complexity. To account for the accuracy of the numerical calculation and at the same time avoid a large number of computations, in this paper, the meshing size of the robot was relatively small, and the meshing size of the cylindrical flow field was slightly larger. The meshing results of the robotic 3D model and the flow field are shown in Fig. 21: the total number of elements was 252,166, and the total number of nodes was 46,810.

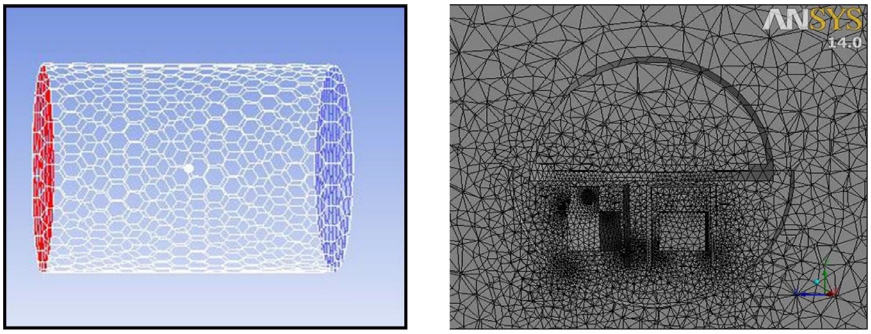

(a) Meshing results of whole area

(b) Details of meshing

Fig. 21. Meshing results of flow field and robot.

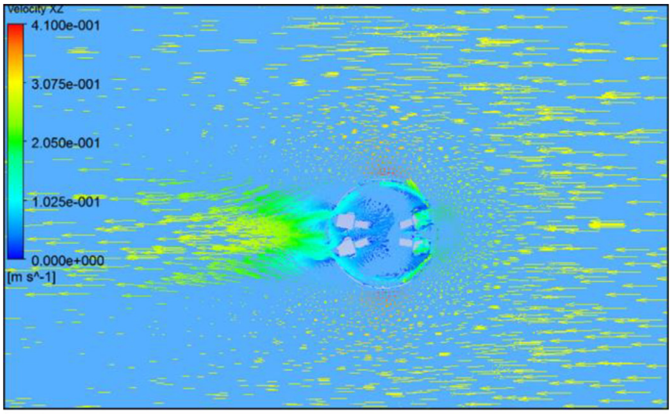

(a) Velocity vectors

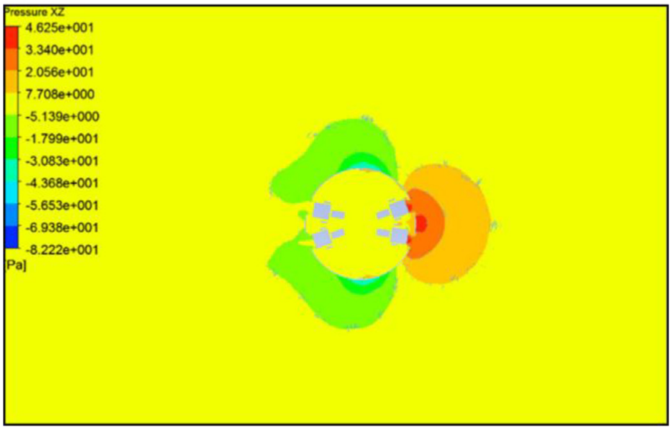

(b) Contours of static pressure

Fig. 22. Results of FLUENT simulation of forward motion.

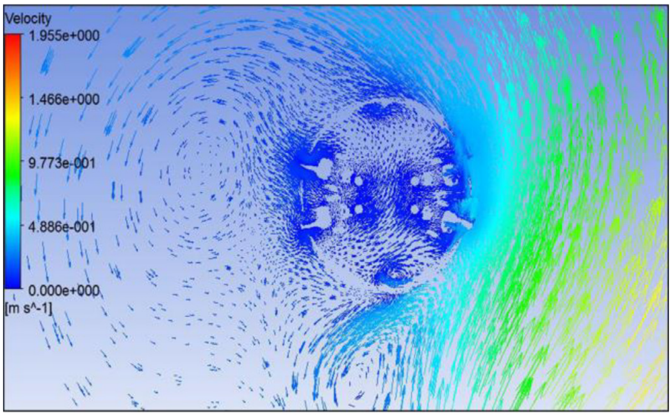

(a) Velocity vectors

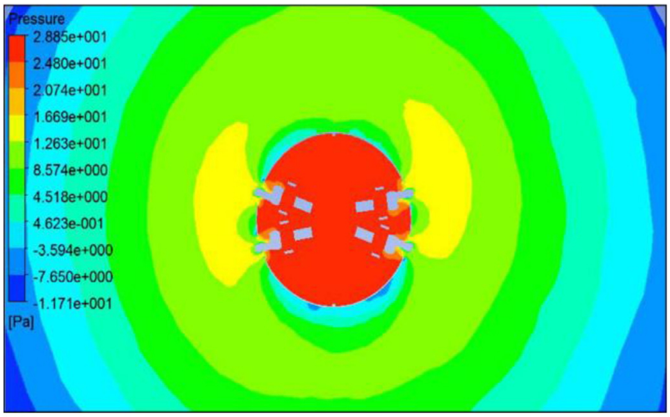

(b) Contours of static pressure

Fig. 23. Results of FLUENT simulation of counter-clockwise motion.

After executing the meshing operation of the amphibious spherical robot and the flow field, four meshing results files were imported into ANSYS FLUENT. According to previous experience and research, it is possible to set the inlet of the flow field as the velocity inlet and the outlet of the flow field as the outflow. In this research, knowing the Reynolds number criterion, it is then possible to establish a k-Ɛ model to perform flow-field simulations, under turbulent conditions. Using this method, we determined that the wall of the amphibious spherical robot was static and that the flow field moves at a certain speed. The convergence criterion in this simulation calculation was 0.0001 [37].

(a) Simulation results of horizontal motion

To simulate horizontal motion underwater, we must consider the propulsive forces generated by the water-jet propeller and the velocity of the flow field, because the robot moves relative to the flow field. This paper considers two types of movement: forward movement and counterclockwise movement. Accordingly, the robot was set as a static wall while the flow field was set with a constant velocity. The velocities of forward movement and counterclockwise movement were 0.3 m/s and 14 rpm, respectively. Past research on movements of amphibious spherical robots adjusted one pair of water-jet propellers to implement different horizontal motions. The propulsion forces of the spherical underwater robot were actuated by two horizontal water-jet propellers for forward movement and counterclockwise movement. From (11), the drag coefficients were 0.61 and 0.099, respectively.

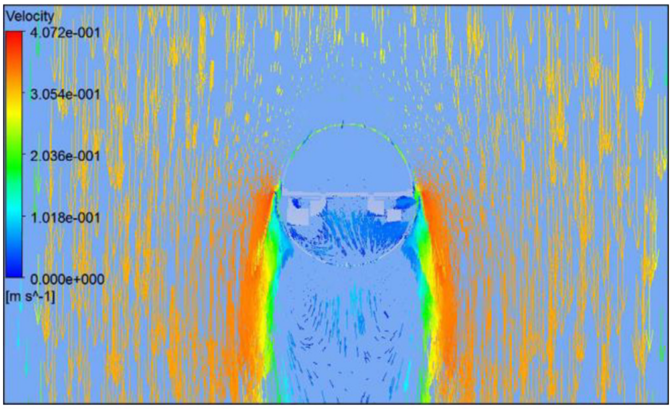

(a) Velocity vectors

(b) Contours of static pressure

Fig. 24. Results of FLUENT simulation of ascending motion.

After hydrodynamic analysis simulations, Fig. 22(a) shows how the velocity of the robot was affected by the flow field. In particular, the effect of the holes was not obvious. Fig. 22(b) shows a cutaway view of the pressure affected by the flow field, Fig. 23 shows the velocity vectors and contours of static pressure for the robot implementing a counterclockwise movement. In the ANSYS FLUENT software, after operating for 1000 steps, the drag coefficients for forward movement and counterclockwise movement were constant, converging to $Cd = 0.579$ and $Cd = 0.079$, respectively; thus, the maximum error between the simulation results and the calculated theoretical values was approximately 5%. Consequently, the results of the ANSYS FLUENT analysis were acceptable [38,39].

(b) Simulation results for vertical motion

In addition to horizontal forward motion and counterclockwise motion, vertical ascending and sinking motions were also simulated in ANSYS FLUENT. In this section, some settings of related parameters were the same as before, the motion of the flow field was also selected as a reference for the motion of the robot in the simulation. From (10), while the robot implements an ascending motion, forces were generated by the four water-jet propellers, and the drag coefficient was 1.2257. Related force and movement mechanisms are illustrated in Fig. 18(c). From the simulation analysis in ANSYS FLUENT, the drag coefficient of vertical ascending motion converged to approximately 1.346.

The interaction between the velocity of the flow field and robot is presented in Fig. 24(a). Moreover, Fig. 24(b) shows that the cross-section of the pressure was affected by the flow field. Next, we estimated the sinking motion of the robot in the vertical plane. Similar to the simulation process above, the drag coefficient for vertical sinking motion converged to approximately 0.0347. The velocity vectors of ascending motion are shown in Fig. 25(a), and the cutaway view of the static pressure contours for sinking motion is shown in Fig. 25(b). With respect to the simulation calculation method, according to (10), the drag coefficient of vertical ascending motion was 0.0332. Through a series of calculations and comparisons, the maximum error of the simulation drag coefficient for vertical motion was approximately 6%, compared with the theoretical calculated value. On the whole, the simulation results of hydrodynamic characteristics based on FLUENT software for horizontal motion and vertical motion were acceptable. More importantly, these simulation results have practical significance.

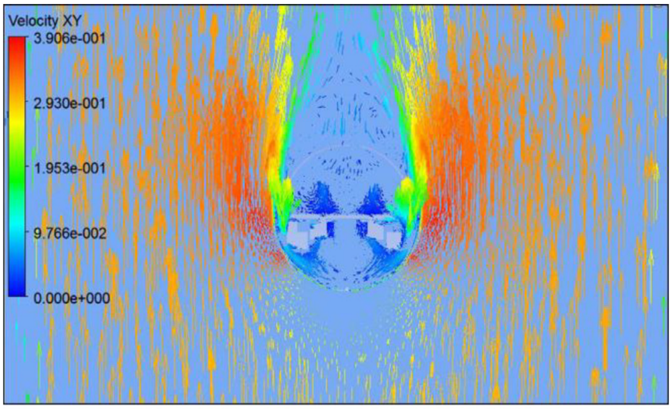

(a) Velocity vectors

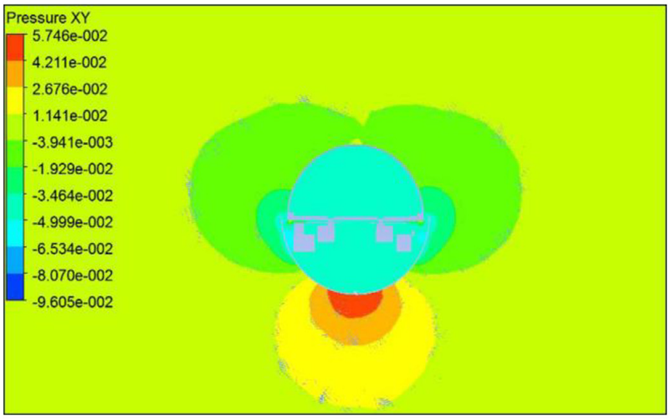

(b) Contours of static pressure

Fig. 25. Results of FLUENT simulation of sinking motion.

This section mainly presented some hydrodynamic analysis of an amphibious spherical robot, and four main basic underwater motions were described and analyzed. To estimate the parameters of dynamic model of robot, we assumed that the robot was a static sphere and the environment of flow field was 20°C without external disturbances. From some simulation results in ANSYS FLUENT, the velocity of the fluid inside the robot was as same as the robot for horizontal and vertical motion. Moreover, the drag coefficient for horizontal and vertical motion were very close to the theoretical values, the maximum error between the simulation results and the desired theoretical values was approximately 5%. Consequently, the fluid inside the robot could be assumed as a part of the robot and the robot could be assumed as a sphere, the results of the ANSYS FLUENT analysis were acceptable and the dynamic equation of the robot could be simplified and optimized. According to these results, we optimized the control strategy of the robot to improve the control accuracy and stability of robot.

5. Experiments on land crawling and underwater swimming

5.1. Experiments on crawling stability

Beyond the kinematic simulations of a virtual prototype of the robot in an ADAMS environment, a series of experiments on walking was also

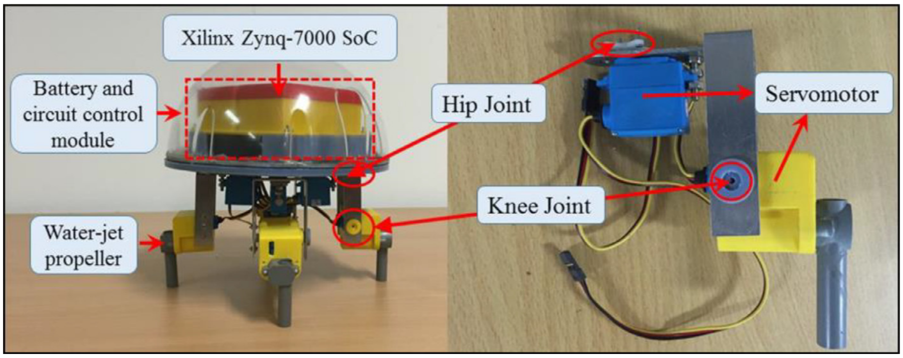

Fig. 26. Prototype of the improved 3D-printed amphibious spherical robot.

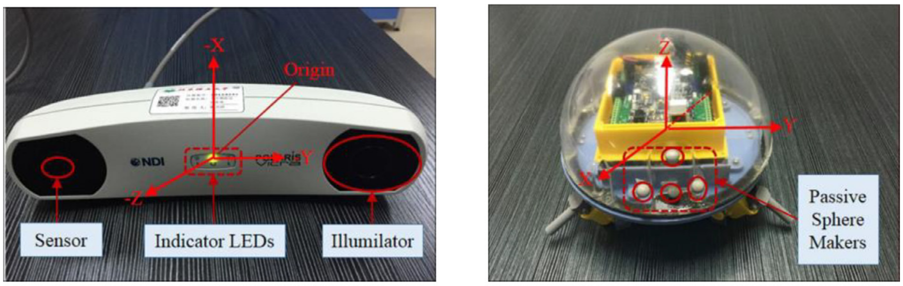

(a) Appearance of NDI

(b) Specific position of sphere markers

Fig. 27. Experimental equipment and related parameters.

carried out on a common mat floor [40]. The crawling gait was adopted, as in the ADAMS simulations, to enhance walking stability. In the crawling gait, a raised leg is set down before the next one is lifted; thus, the timing sequence of the four actuation units must be synchronized to achieve quadruped walking motion. Three or four legs always touch the ground to support the robot and ensure that it remains stable, the prototype and one leg of the improved 3D-printed amphibious spherical robot are shown in Fig. 24.

To obtain more precise experimental results, in this paper a novel optical tracking system, the NDI Polaris Vicra system, was used to evaluate the displacement of the robot. The NDI Polaris Vicra system is an optical measurement system that measures the 3D positions of passive markers. The Polaris Vicra system is able to determine the position and orientation of tools within a specific measurement volume. The whole system includes a position sensor, a host USB converter, a power adapter, and some passive markers. The position sensor is the main component of the NDI system; an overview of its operation is shown in Fig. 27 (left). As can be seen, the position sensor emits infrared light from its illuminators. The infrared light floods the surrounding area and reflects back to the sensor from passive spherical markers, which have a retro-reflective coating to minimize scattering. Passive markers must be attached to the tool using NDI mounting posts, which are manufactured to firmly hold the NDI spheres. Considering the evaluation range of the position sensor, the sensor was positioned at a slightly higher level, allowing it to monitor the motion of the robot from the back; here, four passive spherical markers were used, as shown in Fig. 27 (right).

Because our previous research revealed that the velocity of the robot is related to the step size and the frequency of the gait cycle, here we used a crawling gait and reduced the swing distance for a single step. To avoid the phenomenon of slipping during crawling, the crawling experiments were performed on a common mat, which was also done using the previous robot. Fig. 28 shows a video sequence of crawling. The time and displacement in the crawling experiment were recorded, including the displacement in the forward X direction and deviations in the Y and Z directions. The trajectory curves were generated in MATLAB. The experimental and simulation results are shown in Figs. 29–31. The dashed blue and solid red curves correspond to the experimental results of the previous and the improved robot respectively, while the dash dot green curve indicates the simulation results.

Fig. 29 shows the changes in displacement in the forward direction (X) over time. According to the slope of the experimental trajectory, the crawling speed of the previous robot was less than 0.014 m/s, while the crawling speed of the improved robot was about 0.024 m/s. The experimental results of the improved robot were close to the simulation result of the robotic centroid (0.025 m/s). Fig. 30 shows the deviation in the Y direction. The maximum deviation in the previous robot for the Y direction was 0.14 m, while the maximum deviation in the improved robot for the Y direction was 0.024 m. Furthermore, the changing trends of the improved curve and the simulation curve were approximately consistent. As shown in Fig. 31, the maximum deviation in the improved experimental results for the Z direction was 0.013 m, and the maximum deviation in the previous experimental results was 0.056 m. Consequently, the improved robot has a better performance of on-land crawling than the previous robot.

Compared with the actual experiment, the simulation one was relatively ideal, and there existed some inevitable phenomenon in the actual experiment. In ADAMS simulation, the swing angle of each joint was controlled by the periodic drive function. However, in the actual experiment, it was controlled by adjusting the duty ratio of the PWM control signal, so the control effect in the actual experiment was not as good as simulation. Moreover, there existed some slip phenomenon on the robot's foot end in the actual crawling experiment, which was caused by the delay of control signal. For example, the knee joint may have already started its falling or lifting motion before the hip joint completes its swing motion, which will caused swing angle deviation for joint. And if it was not corrected in time, the deviation will become larger and larger. Thus, the experimental results are not as ideal as the simulation results. Although there was some error between simulation and improved experimental results, there was only a slight deviation, less than 0.013 m, between the actual crawling trajectory and the designated trajectory. The controller module of the robot was set to ignore small deviations. As a result, except for drift occurring at bends in the

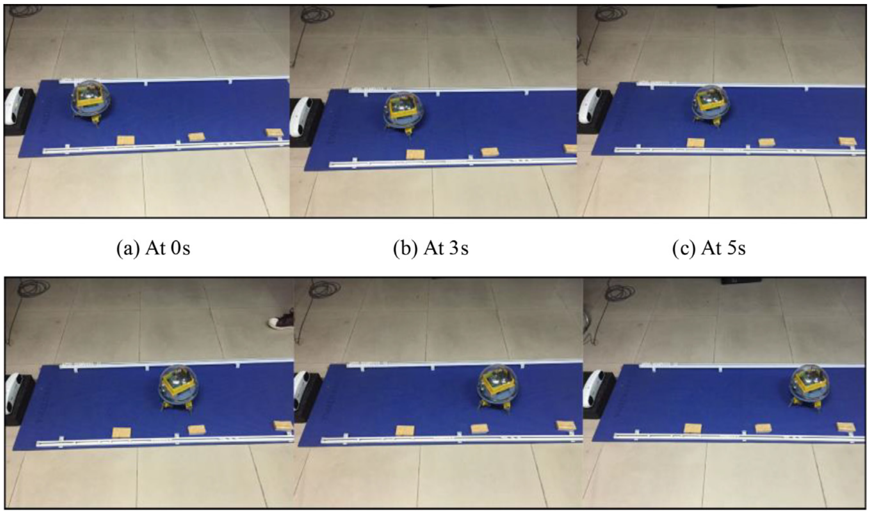

(a) At 0s (b) At 3s (c) At 5s

(d) At 8s (e) At 11s (f) At 14s

Fig. 28. Experiments on crawling stability.

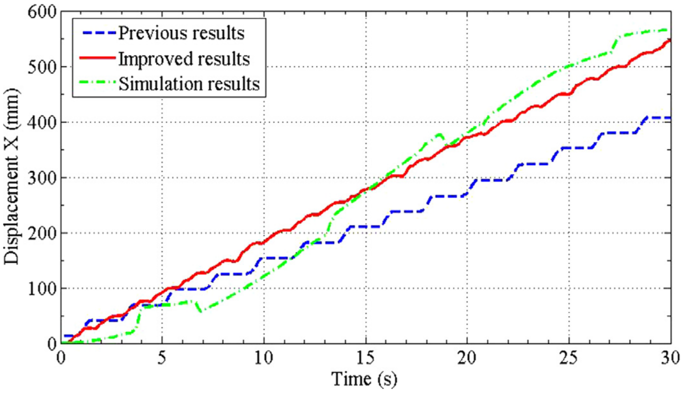

Fig. 29. Displacement in the X direction. (For interpretation of the references to colour in this figure legend, the reader is referred to the web version of this article.)

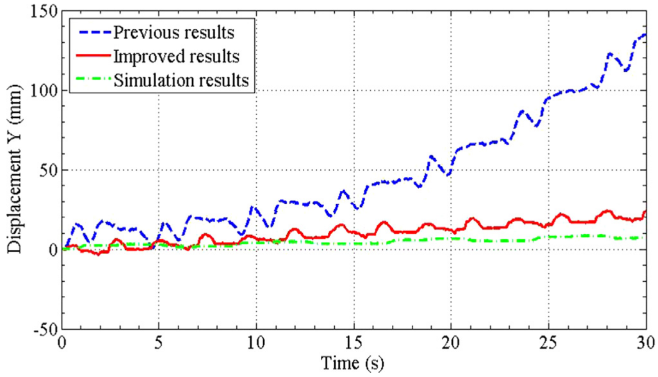

Fig. 30. Displacement in the Y direction. (For interpretation of the references to colour in this figure legend, the reader is referred to the web version of this article.)

designated trajectory, the improved robot was able to follow the trajectory of the initial settings and implement stable crawling. Therefore, the ADAMS software can provide accurate kinematic characteristics and a theoretical foundation for robot control research.

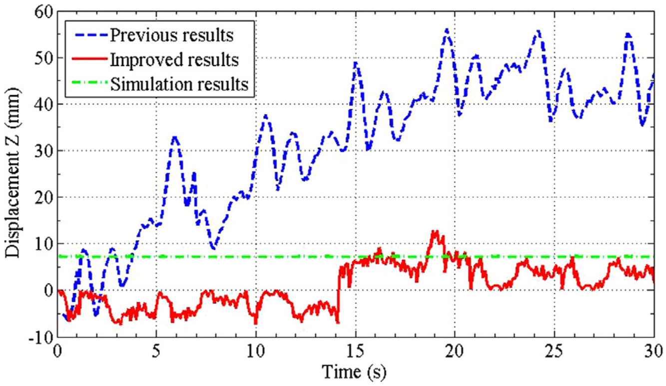

Fig. 31. Displacement in the Z direction. (For interpretation of the references to colour in this figure legend, the reader is referred to the web version of this article.)

5.2. Underwater motion stability experiments

To evaluate the improved amphibious spherical robot, we conducted several underwater experiments in a pool. Firstly, we carried out a horizontal forward motion in a pool, which was also done using the previous robot. These two experiments were carried out by the same control algorithm in a same pool and each one was repeated twenty times. Control signals directed the robot along the desired trajectory and the average velocity was 0.3 m/s. As the robot was symmetrical, the performance was same in the forwards and backwards directions. The robot was programmed to move forward in a distance of 3 m in a pool, and Fig. 32 shows two snapshots of the horizontal forward movement. Fig. 33 shows the displacement and movement time of experiment and simulation. The average velocity of the improved robot was 0.248 m/s, and the previous robot was 0.169 m/s. As shown in the compared results between the experiment and the simulation, the maximum error of the average velocity of the previous robot was about 0.131 m/s. For the improved amphibious spherical robot, the average velocity error was greatly decreased to 0.052 m/s.

In addition to horizontal forward motion, we carried out several experiments for horizontal counter-clockwise rotation motion using the improved and the previous robots. The experiments of rotating continuously were also conducted in the pool, and the angular velocity was measured by an IMU sensor. As show in Fig. 34, the angular velocity of the improved robot was closely coincident with simulation result. More-

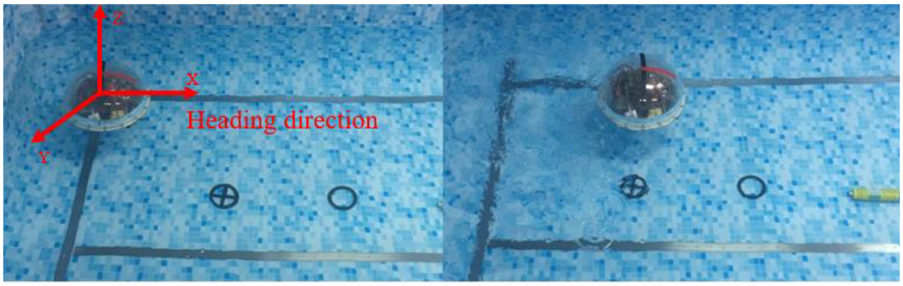

(a) At 0s (b) At 5s

Fig. 32. Underwater horizontal forward motion.

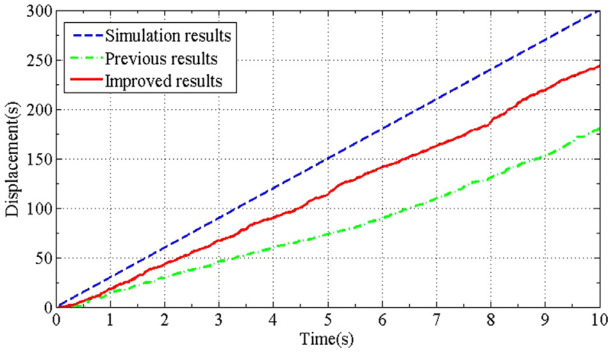

Fig. 33. Experimental results for horizontal forward motion.

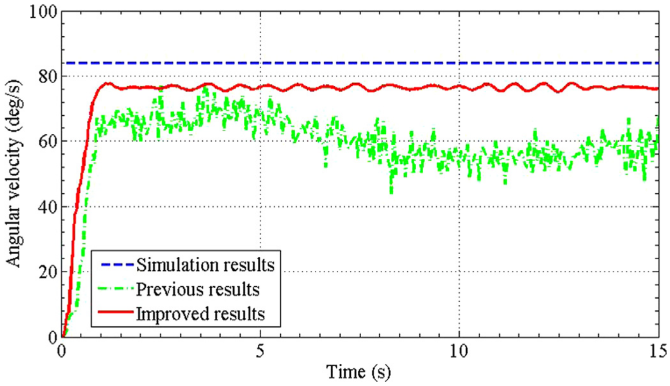

Fig. 34. Experimental results for horizontal counter-clock wise motion.

over, the underwater motion performance of the improved robot was better than the previous one since its angular velocity was more stable. Due to the limitation of pool's depth in experimental condition, it was not sufficient to complete the ascending and sinking motion of robot, hence this paper only shows the performance of horizontal motion.

6. Conclusions

This paper presented the optimization of the kinematic and hydrodynamic model of the amphibious spherical robot, so as to improve the control accuracy and stability of the prototype of robot. Firstly, some on-land kinematic and dynamic modeling parameters, such as the angular velocity and swing angle of each joint, were optimized in ADAMS simulation. Then, while the robot swimming in underwater, the hydrodynamic model of the robot was simplified and optimized in ANSYS-FLUENT simulation and the robot could be assumed as a sphere. Finally, combining the mechanism of the robot with some related simulation results, a prototype of the 3D-printed amphibious spherical robot was built. We carried out some on land crawling experiments and underwater experiments to verify its motion performance, and the compared results demonstrated that the improved amphibious spherical robot was more helpful in enhancing the accuracy of amphibious motion. Moreover, these experimental results not only confirmed the accuracy of the simulation results in describing the kinematic and hydrodynamic characteristics of the robot, but also indicated the deficiency of simulation analysis. In addition, these results provided important guidance to plan the robot's trajectory. Future researches will involve some dynamic on-land gaits and vertical underwater experiments with different frequencies and velocities.

Acknowledgments

This work was supported by National Natural Science Foundation of China (61503028, 61773064). This research project was also partly supported by National Natural Science Foundation of China (61375094) and National High Tech. Research and Development Program of China (No. 2015AA043202).

Supplementary materials

Supplementary material associated with this article can be found, in the online version, at doi:10.1016/j.rcim.2017.11.009.

References

[1] Y. Li, Q. Li, Z. Su, F. Liu, Mechanism design and kinematics simulation of a snake–like amphibious mother-daughter robot with blended-oar-body, Robot 36 (2) (2010) 224–232.
[2] AS. Boxerbaum, P. Werk, RD. Quinn, R. Vaidyanathan, Design of an autonomous amphibious robot for surf zone operation: part I-Mechanical design for multi-mode mobility, in: Proceedings of the IEEE International Conference on Advanced Intelligent Mechatronics, Monterey, CA, 24-28 July 2005, pp. 1459–1464.
[3] J. Yu, R. Ding, Q. Yang, M. Tan, J. Zhang, Amphibious pattern design of a robotic fish with wheel-propeller-fin mechanisms, *J. Field Rob.* 30 (5) (2013) 702–716.
[4] AJ. Ijspeert, A. Crespi, D. Ryczko, JM. Cabelguen, From swimming to crawling with a salamander robot driven by a spinal cord model, Science 315 (5817) (2007) 1416–1420.
[5] S. Guo, J. Du, X. Ye, R. Yan, H. Gao, The computational design of a water jet Propulsion spherical underwater vehicle, in: Proceedings of the 2011 IEEE International Conference on Mechatronics and Automation, Beijing, 7-10 August 2011, pp. 2375–2379.
[6] Y. He, L. Shi, S. Guo, S. Pan, Z. Wang, Preliminary mechanical analysis of an improved amphibious spherical father robot, *Microsyst. Technol.* (2015) 1–16, doi:10.1007/s00542-015-2504-9.
[7] Y. He, L. Shi, S. Guo, S. Pan, Wang Z, 3D printing technology-based an amphibious spherical underwater robot, in: Proceedings of 2014 IEEE International Conference on Mechatronics and Automation, Tianjin, 3-6 August 2014, pp. 1382–1387.
[8] S. Pan, S. Guo, L. Shi, Y. He, Wang Z, Huang Q, A spherical robot based on all programmable SoC and 3-D printing, in: Proceedings of 2014 IEEE International Conference on Mechatronics and Automation, Tianjin, 3-6 August 2014, pp. 150–155.
[9] S. Pan, L. Shi, S. Guo, A kinect-based real-time compressive tracking prototype system for amphibious spherical robots, Sensors 15 (4) (2015) 8232–8252 Apr.
[10] L. Shi, Y. He, S. Guo, Skating motion analysis of the amphibious quadruped mother robot, in: Proceedings of 2013 IEEE International Conference on Mechatronics and Automation, Takamatsu, 4-7 August 2013, pp. 1749–1754.
[11] L. Shi, S. Guo, S. Mao, C. Yue, M. Li, K. Asaka, Development of an amphibious turtle-inspired spherical mother robot, *J. Bionic Eng.* 10 (4) (2013) 446–455.

[12] S. Guo, L. Shi, S. Mao, M. Li, Design and kinematic analysis of an amphibious spherical robot, in: Proceedings of 2014 IEEE International Conference on Mechatronics and Automation, Chengdu, 5-8 August 2012, pp. 2214–2219.

[13] Z. Liu, S. Guo, H. Li, X. Lin, An improved 3D modeling of water-jet propellers for a spherical underwater robot, in: Proceeding of the 2011 IEEE International Conference on Mechatronics and Automation, Beijing, 7-10 August 2011, pp. 319–324.

[14] C. Yue, S. Guo, L. Shi, J. Du, Characteristics evaluation of the vertical motion of a spherical underwater robot, in: Proceedings of 2012 IEEE International Conference on Robotics and Biomimetics, Guangzhou, 11-14 December 2012, pp. 759–764.

[15] Y. Li, S. Guo, C. Yue, Preliminary concept of a novel spherical underwater robot, *Int. J. Mechatron. Autom.* 5 (1) (2015) 11–21.

[16] X. Rong, Y. Li, J. Ruan, B. Li, "Design and simulation for a hydraulic actuated quadruped robot", J. Mech. Sci. Technol. 26 (4), 2012, 1171–1177.

[17] J. Luo, G. Hu, "Study on the simulation of robot motion based on MATLAB", *Journal of Xiamen University Natural Science*, 44 (5), 2005, 640–644.

[18] Y. Zhang, J. Jiang, "Kinematics analysis and simulation study of an archwire bending robot", *Chinese High Technology Letters*, 22 (7), 2012, 727–734.

[19] Q. He, H. Kang, J. Zhu, Y. Xu, "Dynamic mechanical properties of working device of rotary drilling rig under lift-arm luffing conditions", *Journal of Central South University of Science and Technology, Chinese High Technology Letters*, 43 (6), 2012, 2150–2156.

[20] X. Lin, S. Guo, Development of a spherical underwater robot equipped with multiple vectored water-jet-based thrusters, *J. Intell. Rob. Syst.* 67 (3-4) (2012) 307–321.

[21] M. Ueno, Y. Tsukada, H. Sawada, A prototype of submersible surface ship and its Fluid dynamic characteristics, *Ocean Eng.* 38 (14-15) (2011) 1686–1695.

[22] T. Tezduyar, Y. Osawa, Fluid-structure interactions of a parachute crossing the far wake of an aircraft, *Comput. Methods Appl. Mech. Eng.* 191 (6-7) (2001) 717–726.

[23] B. Ji, X. Luo, X. Peng, Y. Wu, H. Xu, "Numerical analysis of cavitation evolution and excited pressure fluctuation around a propeller in non-uniform wake", *International Journal of Multiphase Flow*, Vol.43, pp. 13–21.

[24] C. Yue, S. Guo, L. Shi, Fluid dynamic analysis of the spherical underwater robot SUR-II, *Int. J. Adv. Rob. Syst.* 10 (247) (2013) 1–12.

[25] S. Pan, L. Shi, S. Guo, P. Guo, Y. He, Xiao R, A low-power SoC-based moving target detection system for amphibious spherical robots, in: Proceedings of 2015 IEEE International Conference on Mechatronics and Automation, Beijing, 2-5 August 2015, pp. 1116–1121.

[26] S. Guo, Y. Ji, L. Bi, X. Ma, Y. Wang, A kinematic modeling of an amphibious spherical robot system, in: Proceedings of 2014 IEEE International Conference on Mechatronics and Automation, Tianjin, 3-6 August 2014, pp. 1951–1956.

[27] M. Lou, The virtual simulation of four-footed robot based on the software of ADAMS, *Mod. Manuf. Eng.* 1 (2009) 29–31.

[28] G. Xiong, J. Gao, Z. Xu, J. Lu, Prediction of overcoming berriers for 4*4 mobile robots based on ADAMS, *Comput. Eng. Appl.* 22 (7) (2005) 142–144.

[29] S. You, S. Chen, H. Liang, Kinematics and dynamics simulation of PMT based on ADAMS, *Comput. Simul.* 22 (8) (2005) 181–185.

[30] H. Zheng, J. He, Y. Zhao, X. Tang, Simulation of obstacle avoidance about mobile robot based on ADAMS, *Comput. Simul.* 31 (5) (2014) 336–341.

[31] D. Yu, Y. Qian, Parameter-settings for the dynamic simulation based on ADAMS, *Comput. Simul* 23 (9) (2006) 103–107.

[32] B. Chen, J. Tang, S. Jiang, Kinematics simulation of biomimetic hexapod robot based on ADAMS, *Comput. Simul.* 29 (9) (2012) 182–186.

[33] J. Wang, Y. Zhao, Y. Zhu, Z. Ma, Coordinated simulation of trot gait for quadruped robot based on ADAMS and MATLAB, *Mach. Tool Hydraul.* 43 (3) (2015) 57–59.

[34] L. Shi, S. Guo, C. Yue, Preliminary concept and kinematics simulation of a novel spherical underwater robot, in: Proceedings of 2014 IEEE International Conference on Mechatronics and Automation, Tianjin, 3-6 August 2014, pp. 1907–1912.

[35] M. Li, S. Guo, H. Hirata, H. Ishihara, Design and performance evaluation of an amphibious spherical robot, *Rob. Auton. Syst.* 64 (2015) 21–34.

[36] X. Lin, S. Guo, C. Yue, J. Du, 3D modeling of a vectored water jet based multi-propeller propulsion system for a spherical underwater robot, *Int. J. Adv. Rob. Syst.* 10 (80) (2013) 1–8.

[37] C. Yue, S. Guo, M. Li, ANSYS FLUENT-based modeling and fluid dynamic analysis for a spherical underwater robot, in: Proceedings of 2013 IEEE International Conference on Mechatronics and Automation, Takamatsu, 2013, pp. 1577–1581. 4-7 August.

[38] Y. He, L. Shi, S. Guo, P. Guo, R. Xiao, Numerical simulation and hydrodynamic analysis of an amphibious spherical robot, in: Proceedings of 2014 IEEE International Conference on Mechatronics and Automation, Beijing, 2-5 August 2015, pp. 848–853.

[39] X. Ma, S. Guo, L. Li, Y. Ji, Wang Y, The underwater motion simulation of a spherical amphibious robot, in: Proceedings of 2014 IEEE International Conference on Mechatronics and Automation, Tianjin, 3-6 August 2014, pp. 145–149.

[40] C.P. Santos, V. Matos, Gait transition and modulation in a quadruped robot: a brainstem-like modulation approach, *Rob. Auton. Syst.* 59 (9) (2011) 620–634.